AUTHOR QUERIES

AUTHOR PLEASE ANSWER ALL QUERIES

PLEASE NOTE: We cannot accept new source files as corrections for your article. If possible, please annotate the PDF proof we have sent you with your corrections and upload it via the Author Gateway. Alternatively, you may send us your corrections in list format. You may also upload revised graphics via the Author Gateway.

Carefully check the page proofs (and coordinate with all authors); additional changes or updates WILL NOT be accepted after the article is published online/print in its final form. Please check author names and affiliations, funding, as well as the overall article for any errors prior to sending in your author proof corrections. Your article has been peer reviewed, accepted as final, and sent in to IEEE. No text changes have been made to the main part of the article as dictated by the editorial level of service for your publication.

AQ:1 = Please note that “27-30 GHz” was changed to “27–30 GHz” in the article title to be in compliance with style guidelines.

AQ:2 = Please confirm or add details for any funding or financial support for the research of this article.

AQ:3 = Please provide the publisher name and publisher location for Ref. [29].

AQ:4 = Current affiliation in the biography of Zhangjie Hong does not match the First Footnote. Please check and correct where needed.

AQ:1

A 27–30 GHz T/R Module With Reflection-Type Phase Shifting and Machine-Learned Calibration

Yuan Chang, Yuejiang Wen, *Graduate Student Member, IEEE*,
Zhangjie Hong, *Graduate Student Member, IEEE*, Bharadwaj Padmanabhan, *Graduate Student Member, IEEE*,
Paul D. Franzon, *Fellow, IEEE*, and Brian A. Floyd, *Senior Member, IEEE*

***Abstract*— This paper presents a transmit/receive module (TRM) for phased arrays realized in 45 nm RFSOI CMOS technology and calibrated using machine learning. The 27-30 GHz TRM includes a transmit/receive (T/R) switch, a power amplifier, a low-noise amplifier, another T/R switch, and a bidirectional reflection-type phase shifter (RTPS). The RTPS incorporates multiple resonators and five control variables to achieve a six-bit resolution with a 360-degree phase shift range across a 10% bandwidth. We introduce a machine-learning technique that uses Bayesian optimization to calibrate the multi-variable front end. This technique can attain near-optimal settings with 1.5 percent of the measurements compared to manual calibration using an exhaustive search. Measurements show the TRM achieves 16.4 dB gain, 2.5 GHz 1 dB bandwidth, and 11.9-12.9 dBm output compression point in transmit mode, and 16 dB gain, 3.2 GHz 1 dB BW, −23.3 dBm input compression point, and 4 dB noise figure in receive mode. Across 27-30 GHz, the calibrated TRM achieves root-mean-square errors of 0.4 dB or lower for gain and less than 1.5 or 2.8 degrees for phase in transmit and receive modes, respectively.**

***Index Terms*— Transmit-receive module, beamformer, phased-array, reflection-type phase shifter, millimeter wave, 28 GHz, 5G, calibration, machine learning, Bayesian optimization.**

I. Introduction

PHASED arrays, comprising multiple transmit/receive modules (TRMs), are widely used in millimeter-wave (mmWave) systems [1] to support sensing or high-throughput communications. The phase shifter is a crucial building block influencing the TRM architecture. Active vector-interpolating phase shifters use variable-gain amplifiers for in-phase and quadrature-phase paths [2], [3], [4]. They are unidirectional and usually require the transmitter (Tx) and receiver (Rx) to have separate phase shifters, as shown in Fig. 1(a). In contrast, passive phase shifters can be bidirectional, allowing the phase shifter to be shared by Tx and Rx through transmit/receive (T/R) switches, as shown in Fig. 1(b).

The reflection-type phase shifter (RTPS) is one type of passive phase shifter, where tunable phase shift comes from tuning the reflection coefficient of loads attached to a 90° hybrid coupler. The RTPS can typically realize 180° phase shift range using π-based reflectors. Additional active [3], [5], [6] or passive [7], [8] phase inverters can be cascaded with the RTPS to realize a full 360° phase-shift range. The active inverter compromises power consumption, linearity, and bi-directionality, whereas the passive inverter occupies an area comparable to that of the RTPS itself [7]. Thus, achieving a 360° phase-shift range in a single, compact RTPS design is attractive, with examples found in [8], [9], [10], [11], and [12]. In these examples, additional resonant circuits within the RTPS provide the 360° range, but this comes at the cost of reduced bandwidth (BW) and increased calibration complexity to set multiple control voltages. Both new designs and new calibration techniques are needed.

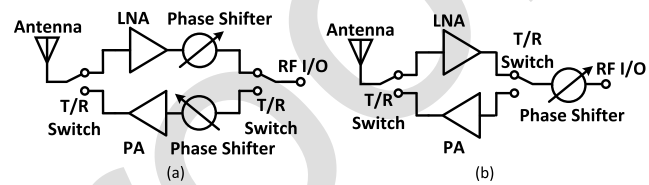

Fig. 1. Block diagrams of transmit/receive modules using either (a) active phase shifters or (b) a passive phase shifter.

In this paper, we present a new 360° phase-shift RTPS design that is incorporated into a 27-30 GHz TRM together with a LNA, PA, and T/R switches. The RTPS is an improved version of our prior work in [13]. Furthermore, we introduce a machine learning (ML) technique to efficiently calibrate the multi-variable circuit and benchmark that approach against a manual approach. The ML approach achieves comparable calibrated performance using 1.5% the number of measurements.

The contributions of this work are summarized as follows:

1) We present a complete TRM with a common 360° RTPS. Most prior RTPS work focuses on stand-alone phase shifters [8], [9], [10], [11], whereas [12] presents an LNA plus RTPS. This paper investigates the RTPS in the context of a complete 27-30 GHz TRM, demonstrating the RTPS's advantages of bi-directionality and compact area.

2) We present a broadband RTPS that uses a single control-voltage look-up table (LUT) to operate over a 10% fractional BW (defined as the frequency range where phase errors are less than half a least-significant bit). Previous 360° phase-shift RTPS designs [9], [10], [11], [12] achieve low gain

AQ:2

Received 17 September 2024; revised 3 December 2024; accepted 27 December 2024. This work was supported in part by the Integrated Device Technology and in part by the National Science Foundation through the Center for Advanced Electronics through Machine Learning (CAEML) under Grant CNS 16-244770. This article was recommended by Associate Editor J. Walling. *(Corresponding author: Brian A. Floyd.)*

The authors are with the Department of Electrical and Computer Engineering, NC State University, Raleigh, NC 27695 USA (e-mail: yuanchang2015@outlook.com; wyuejia@ncsu.edu; zhong3@ncsu.edu; bpadman2@ncsu.edu; paulf@ncsu.edu; brian_floyd@ncsu.edu).

Digital Object Identifier 10.1109/TCSI.2024.3524280

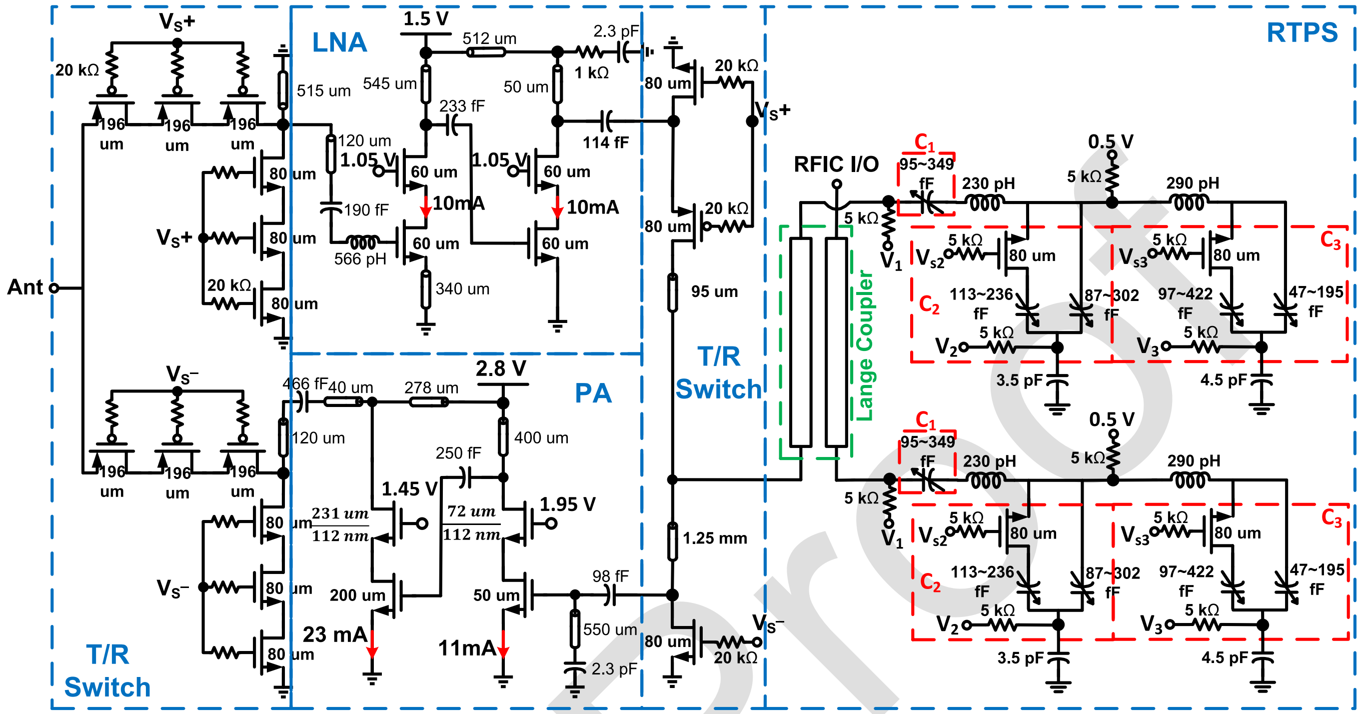

Fig. 2. Schematic of the transmit/receive module (TRM), comprising a transmit/receive (T/R) switch, a low-noise amplifier (LNA), a power amplifier (PA), another T/R switch, and the bidirectional reflection-type phase shifter (RTPS) [13].

and phase root-mean-squared errors (RMSEs) by performing new calibrations at each measurement frequency, making their designs inherently narrow-band. Our broadband RTPS uses a single LUT and can work for wideband modulations and systems having multiple channels. Compared to [14], which also uses only one LUT for the entire band but with π-type reflective loads, our work doubles the phase tuning range, the phase resolution, and the fractional BW in terms of phase RMSE by incorporating an additional resonator into the reflector and by optimally calibrating the circuit.

3) We introduce a new calibration method using surrogate modeling with Bayesian optimization (BO) [15]. This technique efficiently determines the optimum control voltages for six-bit phase resolution across the 27-30 GHz range. To our knowledge, this is the first work that applies BO to phase-shifter calibration. Compared with the exhaustive search, which requires ergodic sweeps of each control setting to select the best, the ML-based calibration attains near-optimal settings with only 1.5% the number of measurements and 15% the amount of time. This calibration allows broadband operation across 27-30 GHz, as highlighted above.

We organize the paper as follows. Section II presents the proposed TRM design, including the radio-frequency front-end (RFFE) and phase shifter details. Section III presents two methods for calibrating the TRM to achieve broadband performance, one using exhaustive search and the other using ML. Section IV presents comprehensive measurement results after calibration and Section V concludes.

II. Transmit/Receive Module Description

A schematic of the TRM is shown in Fig. 2 and includes an RFFE and the RTPS. We implemented the design in GlobalFoundries 45 nm RFSOI CMOS (45RFSOI) technology.

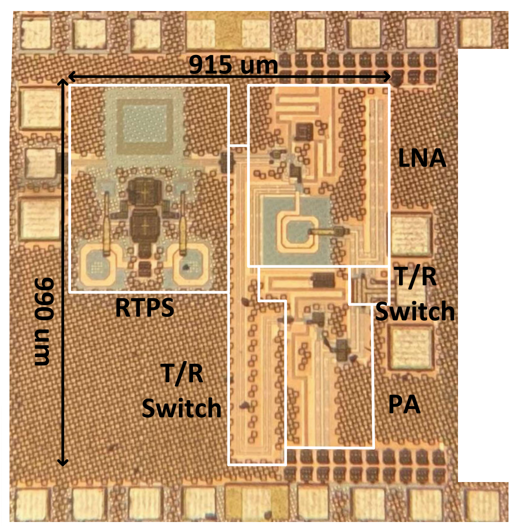

Fig. 3. Die micrograph of the transmit/receive module.

Fig. 2 indicates individual component values, where all transistors use 40 nm channel length unless specifically labeled. Additionally, on-chip transmission lines typically have 50 Ω impedance. Fig. 3 shows a die micrograph of the module. The active area is 0.75 mm^2, excluding pads.

A. RF Front-End

The RFFE includes a T/R switch at the antenna interface, an LNA and PA in parallel, and another T/R switch at the phase-shifter interface. The switch, LNA, and PA designs use standard topologies targeting suitable performance at 28 GHz.

The antenna T/R switch follows a similar design to [16]. We use three-transistor stacks with floating gates and bodies to increase power handling. The floating gates also increase reliability by limiting the fluctuations of gate-to-channel voltages [17], whereas higher gate resistance improves linearity [18]. Simulations at 28 GHz show +25 dBm input 0.1 dB compression point (defined as input power where loss increases by 0.1 dB), 1.1 dB insertion loss (including the routing to the pad and the pad loss) and 26 dB isolation. The parasitics of the switch are absorbed in the input matching of the LNA and the output matching of the PA. Since the maximum signal level is lower at the RTPS interface, we use single-stack transistors for the internal T/R switch. Furthermore, we use a quarter-wave transmission line instead of a series switch in the TX path. For this internal T/R switch, simulations at 28 GHz in TX (RX) modes show 16.6 (16.5) dBm input 0.1 dB compression, 0.5 (1.0) dB insertion loss and 35 (22) dB isolation.

The PA is a two-stage design using cascodes with thick-oxide transistors for the top, common-gate, devices. The pre-driver is biased in the Class-A region, whereas the output stage is biased in Class-B. Simulations show that power gain and output-referred 1 dB compression point (oP_{1dB}) are 26 dB and 15.5 dBm, respectively, with peak power-added efficiency (PAE) of 33%. The LNA is a standard two-stage cascode achieving 23.5 dB gain and 2.3 dB noise figure (NF), although lower NF is possible for this technology.

We fabricated and measured a breakout circuit of the RFFE. Measurement results at 28 GHz are summarized below, with simulation results in parentheses. The TX RFFE achieves 23.5 (24.2) dB peak gain, 2.5 (2.7) GHz 1 dB BW 12 (14) dBm oP_{1dB}, 13 (15) dBm saturated output power (P_{sat}), and 13.0% (17.5%) peak PAE. The RX RFFE achieves 23.5 (22.0) dB peak gain, 3.2 (4.5) GHz 1 dB BW, −21 (−19.4) dBm input-referred 1 dB compression point (iP_{1dB}), and 3.8 (3.7) dB NF.

B. Reflection-Type Phase Shifter

The RTPS is an improved version of our prior work in [13]. As shown in Fig. 2, the RTPS includes a 90° hybrid coupler terminated with tunable reflector loads at the through and coupled ports. We include a summary of the critical components of the RTPS here and direct readers to [13] and the Appendix for additional details.

Coupler The hybrid uses a spiral Lange coupler topology, as shown in Fig. 4. Horizontal coupling between wires [11], [19] increases the even- to odd-mode characteristic impedance ratio. The spiral structure conserves area and avoids the negative mutual inductance encountered in zig-zag layouts. Across 24-34 GHz, electromagnetic simulations of the coupler using Momentum indicate through and coupled port responses of −3.5±0.55 dB with 88.4° to 90.2° phase difference. Isolation is >24 dB and return loss is >28 dB.

Reflectors The reflectors are realized using an L-C series resonant circuit followed by a C-L-C π network. The π network provides a 180° phase shift range, whereas the series L-C circuit provides an additional 180° phase shift.

We explain the reflector operation using the Smith chart in Fig. 5. This depicts the reflection coefficient of the load at a single frequency as the varactor control voltages are varied to

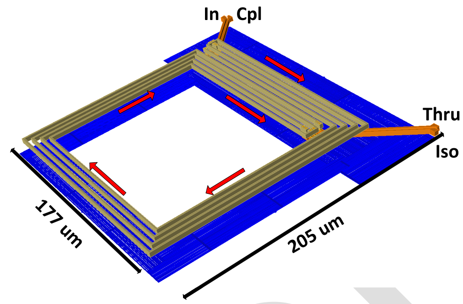

Fig. 4. Drawing of the spiral layout of the Lange coupler, where the red arrows indicate current directions [13].

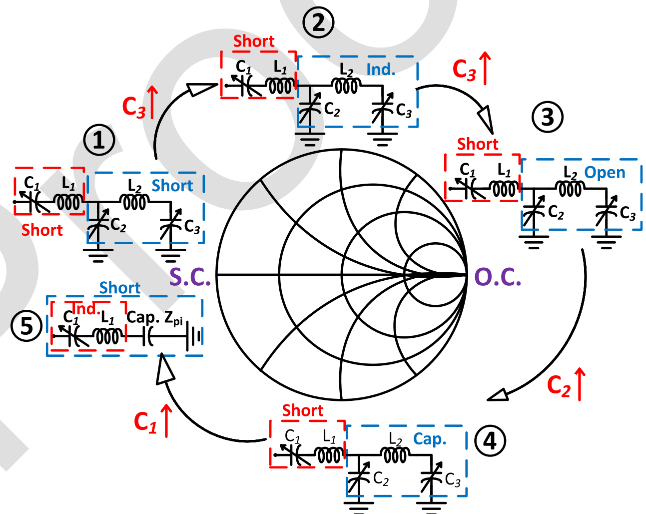

Fig. 5. States of the reflective load, which includes a π network (blue dashed box) and a series LC (red dashed box) [13].

achieve the indicated states. For states 1-4, the leading L-C series network is kept in series resonance, and the overall load behaves like the original π network. Movement between states 1-3 is controlled by tuning of C_3 to control the π network to be a short circuit in state 1, inductive in state 2, and an open circuit in state 3 (meaning the L_2-C_3 combination becomes inductive and resonates with C_2). In state 4, we increase C_2 to make the π network capacitive. Finally, in state 5, we increase C_1 such that C_1-L_1 becomes inductive and resonates with the capacitive π network to achieve a full 360° phase-shift range.

Importantly, C_1 provides a degree of freedom that increases the BW of the reflector. Through tuning of C_1, the load's magnitude response can be kept uniform across a wider frequency range, as shown in our prior work (see Fig. 3 in [13]). For example, we can reduce the leading reactance to lower the reflection coefficient at higher frequencies and stay on a constant magnitude trajectory.

Each reflector includes three varactors and two inductors. Varactors employ thin-oxide accumulation-mode MOS capacitors controlled using continuous (analog) voltages.[1] These varactors have a tuning range between 2:1 and 4:1 with parasitic resistance between 3-10 Ω. To increase the tuning

[1] As we will show through measurement, these varactors would be better off implemented as digitally controlled capacitors to improve linearity.

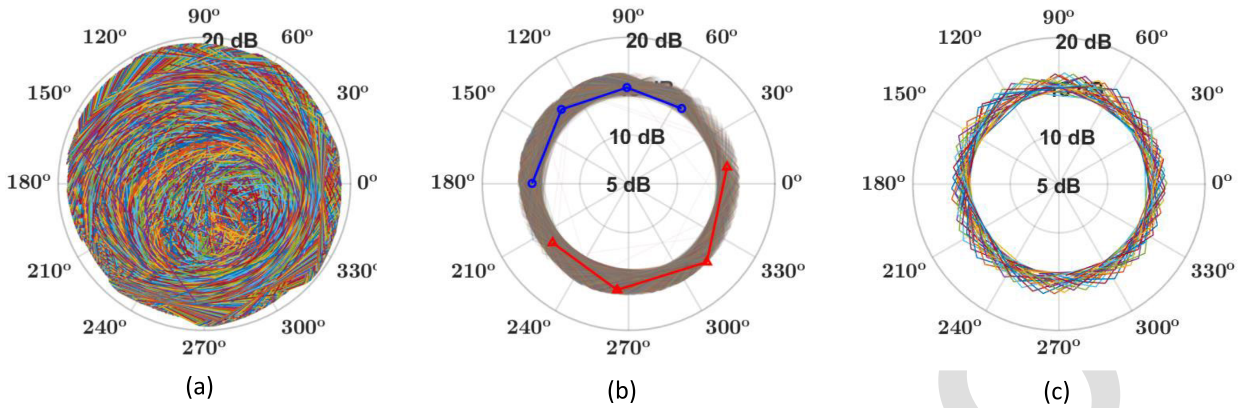

Fig. 6. (a) Measured S_{21} of the TRM in TX mode across frequency at all possible voltage settings. The center of the polar plot indicates minimal gain, *i.e.*, notches. (b) S_{21} at the initial pruned voltage settings providing "flat" (14.4-16.4 dB) amplitude responses. The blue curve with circle markers and the red curve with triangle markers indicate nonuniform and uniform phase responses, respectively. (c) S_{21} at the selected voltage settings that minimizes the phase RMSE across the band.

range, both shunt varactors in the π network include switches to incorporate additional varactors in parallel. The circuit has five control voltages–three continuous and two discrete.

Regarding inductors, L_2 (290 pH) is implemented using 15 μm wide metal to achieve a high quality-factor (Q) of 29, which is necessary to reduce loss at shunt resonance. L_1 (230 pH) is implemented using 2 μm metal to achieve a more compact layout with Q of 19. Lower Q for L_1 does not degrade performance since the overall insertion loss is mainly limited by the resistances of shunt resonance [9]. The self-resonance frequencies of L_2 and L_1 are 74 and 130 GHz, respectively– much higher than our operating frequency.

III. Calibration Methods

A primary challenge in circuits employing an RTPS is developing accurate and broadband calibrations. We evaluated two calibration methods to determine the optimum settings of our five control voltages. One method used an exhaustive search [13], and the other used machine learning (ML). Our goal is to calibrate the TRM by finding a *single* LUT that covers the entire 27-30 GHz band in both TX and RX modes, in contrast to narrowband RTPS work [9], [10], [11], [12] that use different calibrations at different frequencies.

A. Calibration Using Exhaustive Search

We first calibrated the TRM using an exhaustive search method to evaluate all possible states of the TRM across frequency and select the optimum control values. This also serves as a benchmark for the ML calibration. In this design, on-chip digital-to-analog converters (DACs) were not included; thus, we control off-chip supplies to mimic a DAC response. The three continuous voltages (V_1, V_2, V_3) sweep between 0 and 1.5 V in 30 mV steps, and the two discrete voltages (V_{s2}, V_{s3}) toggle between OFF and ON states. In contrast to [12], the control voltages for both reflectors in our RTPS are always controlled symmetrically. The exhaustive search method utilizes $2 \times 2 \times 51 \times 51 \times 51 = 530,604$ voltage sweeps, taking 40 hours using a vector network analyzer.

We use a two-step data pruning from [13] in the calibration. First, we evaluate all possible S_{21} frequency responses for the TRM in TX mode, with results shown in Fig. 6(a). The figure indicates a full 360° phase-shift range but with a wide range of possible gains. Therefore, we prune this data for gains within a target range of 14.4-16.4 dB, as shown in Fig. 6(b). As a result, gain RMSE will meet the target, but multiple potential phase responses remain. In Fig. 6(b), two example curves are indicated–one in blue showing a nonuniform phase response across frequency and one in red showing a uniform phase response across frequency. If nonuniform responses are selected, then the TRM would show poor phase RMSE at band edges, resulting in narrower BW for the TRM. Thus, we prune the data again to select responses with uniform phase progressions across the band for six-bit phase resolution, as shown in Fig. 6(c). The measurement section shows that the minimum phase and gain RMSE are below 1° and 0.3 dB for the exhaustive search calibration.

B. Calibration Using Machine Learning

We also pursued a calibration technique that used ML to evaluate its speed and accuracy compared to the exhaustive search. Specifically, we used a method based on Bayesian optimization (BO) to determine the five control voltages for broadband operation. BO is a sample-efficient statistical optimizer for complex functions where the relationship between input variables does not have to be linear or independent [20], and the relationship between the input and the output does not have to be well understood or accurately modeled [21], [22], [23], [24], [25]. These benefits match the TRM calibration goal, allowing BO to efficiently capture the complex relationships between the control voltages and vector response. BO has been previously used in circuit applications, such as analog circuit synthesis [26] and post-silicon tuning of operational amplifiers [24], [27] and power amplifiers [28]. Here, we apply a customized BO to phase-shifter calibration for the first time.

BO is a sequential model-based optimization described in Algorithm 1. It has an efficient sampling strategy guided by the predictions of a surrogate model. Also, BO manages noise and uncertainty. The result is fewer measurements with the flexibility to incorporate phase-shifter knowledge to choose suitable models and sampling methods to fine-tune results.

Algorithm 1 Bayesian Optimization

```
Input: Initial set of observations D_0, maximum iterations
    T, search region R.
Output: the optima results: (v_opt, Min(ε)).
initialization: v ∈ R = [ ], t=0
while t < T do
    Finding v_{t+1} to make arg max_{v_{t+1}∈R}(metric$(v_{t+1}))
    Measurement of objective function ε_{t+1} = F(v_{t+1})
    Updating surrogate model on augmented dataset: D_t ∪
        (v_{t+1}, ε_{t+1})
end while
return best results (v_opt, Min(ε))
```

$The acquisition metric is a (surrogate model predictions of function value and uncertainty), where a is the acquisition function.

There are three elements to the BO approach: the objective function, the surrogate model, and the acquisition function. The objective function meaningfully combines performance goals of the circuit. The surrogate models the TRM's relationship between input control voltages and the objective function. This model, in turn, is used to construct an acquisition function that determines points to evaluate, aiming to approach the global optimum efficiently. Each new query point is used to refine the surrogate model [31]. Finally, this iterative process continues until the algorithm converges or the number of iterations reaches its restricted number.

In contrast to the exhaustive search method, here, we allowed the resolution of V_1, V_2, and V_3 to be 0.4 mV, limited by the external voltage sources used in the measurement. This was done to evaluate whether improved performance for ML was possible without incurring the time penalty of an exhaustive search having to evaluate these finer steps. Overall, the ML calibration time is constrained by the objective function and the iteration limit.

1) Objective Function: Our goal for the TRM is to achieve accurate element magnitude and phase responses over a desired BW for a desired phase resolution. The objective function is therefore selected as the root mean squared (RMS) error vector magnitude (EVM) across the band, defined as[2]

$$\epsilon(p, \boldsymbol{v}) = \sqrt{\frac{1}{7}\sum_{n=1}^{7}\left|S_{21_{target}}(\omega_n, p) - S_{21_{meas}}(\omega_n, \boldsymbol{v})\right|^2}, \quad (1)$$

where p is the phase index, $\boldsymbol{v} = [V_1, V_2, V_3, V_{s2}, V_{s3}]^\top$ is an input vector of control voltages, and $n = 1, 2 \ldots 7$ represents frequency points uniformly distributed across 27-30 GHz. For our objective function, accuracy is assessed using EVM, defined as the magnitude difference between the target and measured S_{21} for each phase state. BW is assessed using RMS averaging of EVM across frequency, where the mean-squared function accentuates large errors such that the overall broadband performance can be more uniform. Details on how this objective function connects to the actual circuit behavior are provided in section A of the Appendix.

[2]The RMS-EVM is an average across frequency and is evaluated for each phase state. This is in contrast to gain and phase RMSE, which averages across phase states and is evaluated for each frequency.

The optimization goal is to minimize ϵ for each phase state, p. This requires TRM-specific circuit knowledge in setting both the target magnitude and phase across frequency. These can come from either simulations or initial measurement data. In our work, we set our initial goal using a single manually calibrated phase state. All other goals are relative to this result, where each objective function will have a phase goal decremented by the desired phase step (e.g., 5.625° for six-bit resolution). We are investigating alternatives for finding this initial goal, including performing an initial coarse calibration or using simulation results.

2) Surrogate Model: We use a Gaussian process (GP) for the non-parametric surrogate model of the TRM's objective function, ϵ. Each phase state has its own surrogate model; hence, 64 models are trained for six-bit resolution. GP has few assumptions of the underlying function [29], [30], [31], allowing it to adapt to the complexity of the calibration process.

The GP is specified by its mean and variance, with details provided in the Appendix. First, a quadratic mean function empirically models the relationship between voltage settings and the objective function [30]. According to our experiments, quadratic mean functions outperform constant and linear mean functions. Second, the covariance matrix, specified by a kernel, defines the correlation and uncertainty between different points in the search space to estimate function value and uncertainty of nearby untested solutions. We select a Matérn kernel [32] and assume the function to be stationary over the search region and smooth with continuous first derivatives. These assumptions improve the generalization and accuracy of model predictions because the RTPS behavior remains consistent in most search regions. However, the mean or variations in some regions may differ, degrading the model. Our later discussions on global and local search will address this problem.

3) Acquisition Functions: The acquisition function is critical for determining the points to sample within a large search space. Notably, the physics-based behavior of the circuit (e.g., the resonances discussed in Fig. 5) is not used to acquire new data points. Instead, the algorithm acquires new points based on weighted combination of exploration and exploitation criteria. Exploration refers to seeking new data points in regions with high variations, whereas exploitation refers to seeking points in regions where the current model of the objective function is optimized. Different acquisition functions have different abilities [33] in balancing these two components. Our work uses batch-sampling strategies [34] in each iteration, combining the moment-generating function of improvement [33] (initially, more explorative, and then, more exploitative), the epsilon-probability of improvement [35] (more exploitative), and the upper confidence bound [36] (controlled trade-off between exploitation and exploration) [37].

Each iteration samples a batch of points using these different acquisition functions, and all samples in the batch are augmented to the existing dataset to update the surrogate model for the next sampling, as explained in Algorithm 1 and the Appendix. For initialization, Latin hypercube sampling replaces random sampling for constructing the initial surrogate model [38] to ensure that points are evenly distributed in equal intervals of the search space.

4) Iteration and Convergence: With the TRM measurement objective, each vector across 64 phase settings (*i.e.,* six-bit) is measured and optimized sequentially by tuning the five control voltages and learning different GP surrogate models for each phase setting. The RMS-EVM results can be either smooth (the GP shares the same mean and variation) or rough (the objective function undergoes significant changes, and the statistical properties (e.g., the mean and variance) of the models vary, such as when the switch voltage changes from OFF to ON). If rough, the surrogate model with prior statistical assumptions may struggle to adapt quickly, particularly within large search spaces with noisy conditions.

To handle such problems, global and local searches are combined to approach the optimum, as detailed in Algorithm 2. Global search first explores the entire solution space using more explorative acquisition to find regions that may contain an optimum. If the RMS-EVM from the global search for a target phase is below our threshold ($\epsilon_{threshold}$) then the global search result is used as the final result. If the goal is unmet, a local search commences [37], using more exploitative acquisition. The local search area is defined by overlapping the globally-determined control voltages (v_{global}) of adjacent phase states, expanded by a voltage range, r. If there is a failed convergence, then r is increased. Otherwise, r is narrowed to iteratively approach an optimum ($v_{precise}$).

C. Calibration Results and Comparison

S-parameter results of the TRM will be detailed in Section IV. Here, we first compare the calibration methods in terms of RMSE performance across frequency for both Tx and Rx. Fig. 7 depicts virtually identical results, with gain RMSE <0.4 dB across 27-30 GHz and phase RMSE less than 1.5° or 2.8° in Tx and Rx modes, respectively. At some frequencies, the ML method achieves slightly lower RMSE than the exhaustive search, because of its finer control-voltage resolution (0.4 mV, limited by the voltage sources).

We also compare the methods in terms of implementation and calibration time. The exhaustive search used LabView to control instruments and Matlab to process data, whereas the ML method used LabView to control instruments and Python to run all BO scripts. ML calibration required 1.5% of the total measurements and 15% of the measurement time needed by the exhaustive search. Specifically, the manual calibration took 530,604 sweeps and 40 hours, whereas the ML calibration took 7977 sweeps and 5.9 hours (with 4725 sweeps in a global search and 3252 sweeps in a local search).[3] To explore the accuracy and speed trade-off in ML calibration, we compared calibrations for six-bit and five-bit phase resolution in Tx mode. The five-bit response has half as many states to calibrate and targets an error threshold that is doubled. Table I shows that both gain and phase RMSE values are almost double the six-bit results, as expected, with a 3.4X reduction in the number of sweeps and a 4.5X reduction in calibration time.

In summary, compared with the exhaustive search method, the ML method achieves virtually identical RF performances but with a 6.8X reduction in calibration time. If lower accuracy is allowed, calibration time will be reduced accordingly. Further calibration time reduction can be achieved through software optimization, running all code in the same environment.[4] Thus, the ML-based method is preferable when computational resources are available but time is limited.

[3]The experiments were conducted on a computer equipped with an Intel Core i7-7700 processor (4 cores, 8 threads, 3.6 GHz base frequency), and 16 GB of DDR4 RAM.

Algorithm 2 Global+Local Bayesian Optimization

Input: Initial set of observations D, maximum iterations T, search region R.
Output: List of precise local optima $\{v_{\text{precise}_1}, v_{\text{precise}_2}, \ldots, v_{\text{precise}_{64}}\}$.
initialization: $v_{\text{global}} = [\ ]$, $v_{\text{precise}} = [\ ]$, $R'_{local} = [\ ]$
for each $p = 1, 2, 3, \ldots, 64$ **do**
  $t = 0$
  while $t < T$ **do**
    BO training on augmented dataset$^{\$}$: $\mathcal{D}_{t+1}$ in R
  end while
  BO outputs v_{global_p}
end for
for each $p' = 1, 2, 3, \ldots, 64$ **do**
  if $\epsilon(v_{\text{global}_{p'}}) < \epsilon_{threshold}$ **then**
    $v_{\text{precise}_{p'}} = v_{\text{global}_p}$
  else
    $R' = (v_{\text{global}_{p'}} \pm r) \cup (v_{\text{global}_{p' \pm i}} \pm r)$ $(i = 1, 2, 3, 4)$
    $t' = 0$
    while $t' < T$ **do**
      BO' training on augmented dataset$^{\$}$: $\mathcal{D}'_{t+1}$ in R'
    end while
    BO' output $v_{\text{precise}_{p'}}$
  end if
end for
return $\{v_{\text{precise}_1}, v_{\text{precise}_2}, \ldots, v_{\text{precise}_{64}}\}$

$^{\$}$See Algorithm 1, lines 5-7.

TABLE I
ACCURACY VS. SPEED IN ML CALIBRATION

LSB (°)	$\epsilon_{threshold}$ (V/V)	RMSE (dB)	RMSE (°)	Num. of Sweeps	Time (hours)
5.625	0.5	< 0.4	< 1.5	7977	5.9
11.25	1	< 0.7	< 3.1	2367	1.3

[4]Each sweep of the ML routine takes ~2.7 s on average after initial random sampling, with 0.9 s used for measurement and read/write time through the COM interface between LabView and Python. The interfacing time could be eliminated by porting the control and algorithm software to the same environment.

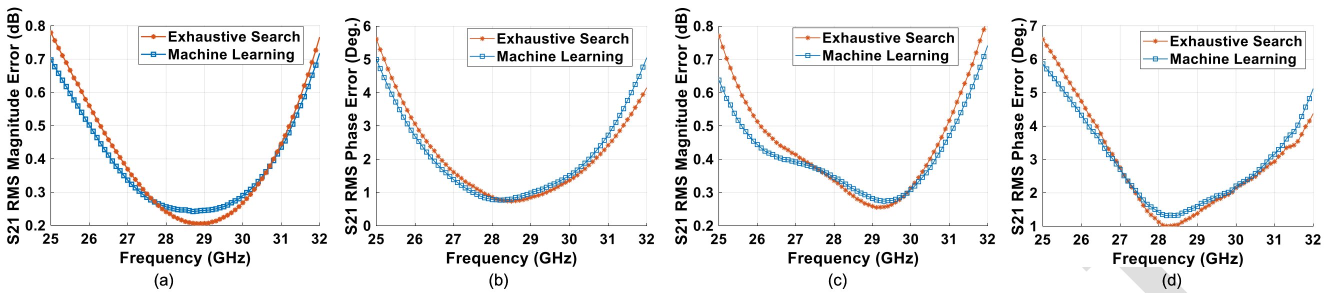

Fig. 7. Measured root-mean-squared error (RMSE) comparison across frequency between manual and machine learning calibrations of the TRM for (a) TX gain, (b) TX phase, (c) RX gain, and (d) RX phase.

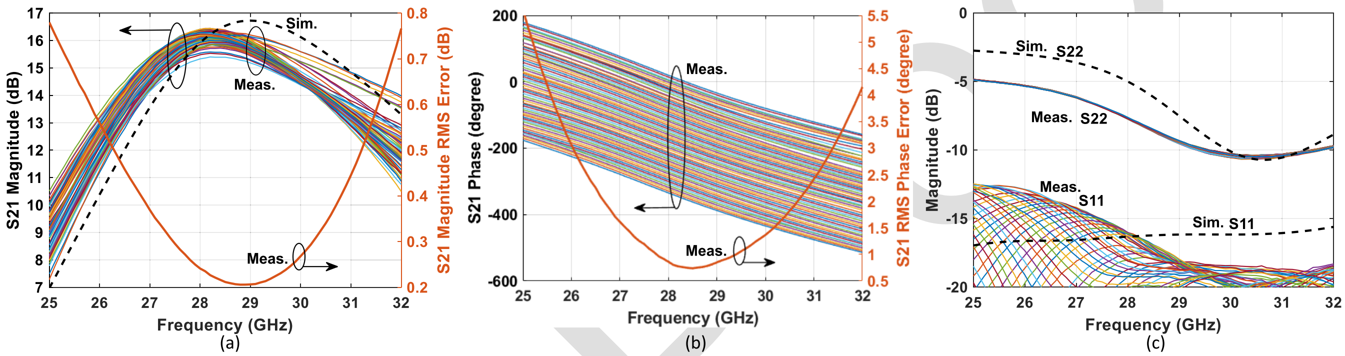

Fig. 8. Measured TX results across all 64 phase states after calibration in TX mode: (a) S_{21} magnitude and RMSE, (b) S_{21} phase and RMSE, and (c) S_{11} and S_{22}. The dashed black curves represent the simulated average values across all settings.

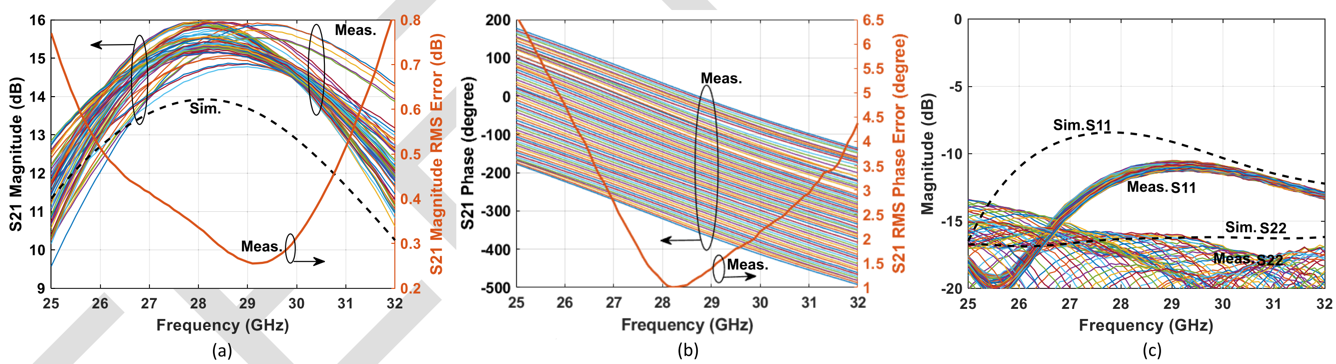

Fig. 9. Measured RX results across all 64 phase states after calibration in TX mode: (a) S_{21} magnitude and RMSE, (b) S_{21} phase and RMSE, and (c) S_{11} and S_{22}. The dashed black curves represent the simulated average values across all settings.

IV. Measured Results After Calibration

After the manual and ML calibrations, two optimal LUTs are obtained. As demonstrated in Fig. 7, these tables are virtually identical; hence, we only present comprehensive measurements for the exhaustive search results. We measured the s-parameters, NF, and linearity of the TRM in both TX and RX modes after a TX-only calibration. The same LUT is also used to control the phase shifter in RX mode.

The measured TX s-parameter performance across frequency provided by this optimal LUT is shown in Fig. 8. Fig. 8(a) shows a peak gain of 16.4 dB and a 1 dB BW of 2.5 GHz. The gain RMSE achieves a minimum value of 0.2 dB at 28.9 GHz and is <0.4 dB across 27-30 GHz. Fig. 8(b) shows the circuit achieves a full 360° phase-shift with six-bit resolution. The phase RMSE achieves a minimum value of 0.7° at 28.5 GHz and is less than 1.6° across the band. Fig. 8(c) shows suitable input matching at the RTPS side and invariant output matching at the antenna side across phase settings. Simulation results are overlaid, showing agreement.

We use the same voltage settings to measure RX s-parameters. The peak gain is 16 dB, as shown in Fig. 9(a). Although the peak gain frequencies are shifted for some phase settings, the gain is within 1 dB of the peak across the whole band. The gain RMSE achieves a minimum value of 0.25 dB at 29.2 GHz and is <0.4 dB across the band. Fig. 9(b) shows that the RX also achieves a full 360° phase-shift with six-bit resolution. The phase RMSE achieves a minimum value of 1° at 28.3 GHz and is <2.8°, which is half of the least-significant bit (LSB), across the band. Fig. 9(c) shows suitable output matching at the RTPS side and invariant input matching at the antenna side across all phase settings. A comparison of gain measurements between the front-end without RTPS and the full TRM indicates that the RTPS has 8 dB insertion loss.

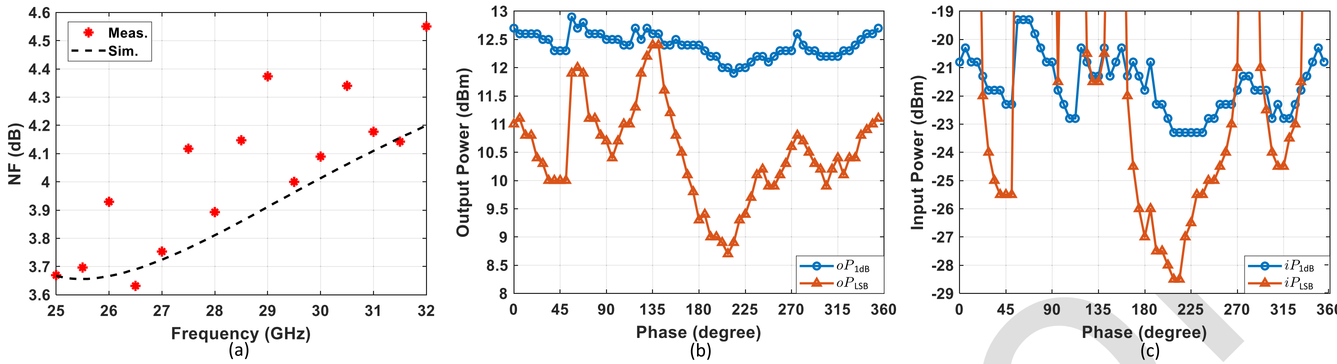

Fig. 10. Results of the TRM after calibration, showing (a) measured and simulated RX NF at the lowest gain phase setting, (b) measured TX oP_{1dB} and oP_{LSB}, and (c) measured RX iP_{1dB} and iP_{LSB}.

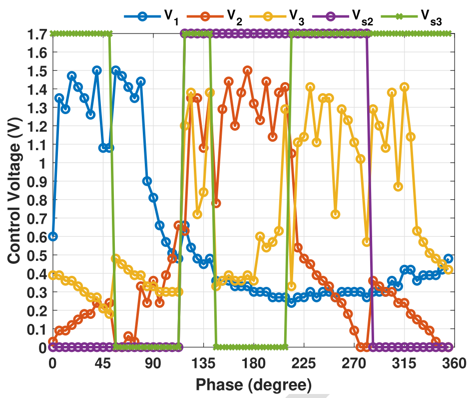

Fig. 11. Gate-voltage settings for the RTPS obtained after calibration. The body of each varactor is biased at 0.5 V.

As shown, the LUT from the TX calibration also works for RX, though RMSE is slightly degraded. This is due to slight differences in impedance in RX and TX modes at the front-end/RTPS interface. If the calibration was instead performed in RX mode, then more accurate RX RMSE would be achieved.

We measured the NF and linearity for these calibrated settings. Fig. 10(a) shows the NF in RX mode at the *lowest* gain phase setting, *i.e.*, worst-case NF. The NF varies between 3.7 dB and 4.1 dB with ±0.1 dB uncertainty due to de-embedding and uncertainty in the noise source's excess noise ratio. The average NF is 4.0 dB, agreeing with the simulation.

For linearity, we evaluate both amplitude modulation (AM) and phase modulation (PM) distortions. The AM distortion is evaluated using iP_{1dB} and oP_{1dB}. The AM-PM distortion is evaluated by measuring the power level at which the S_{21} phase deviates by the LSB of the phase shifter, equal to 5.625° for 6-bit resolution. This is termed input-referred phase compression point by one LSB (iP_{LSB}) or output-referred phase compression point by one LSB (oP_{LSB}). Below these power levels, at least a five-bit effective phase resolution is achieved. Fig. 10(b) shows TX oP_{1dB} and oP_{LSB} across phase settings at 28 GHz. oP_{1dB} varies between 11.9 dBm and 12.9 dBm, whereas oP_{LSB} varies between 8.7 dBm and 12.4 dBm. Fig. 10(c) shows linearity measurements in RX mode, where iP_{1dB} varies between −23.3 dBm and −19.3 dBm, and the lowest iP_{LSB} is −28.5 dBm.

We see large AM-PM distortion, limiting the overall power handling or the phase shifter resolution. Without sufficient power back-off, the beam pattern would fluctuate as a function of the envelope power. This is due to using varactors in the reflectors, where the voltage swing at the reflector will lead to shifts in the reflection coefficient from the RTPS loads. To further debug this issue, we evaluate the control voltages for the phase settings with the poorest phase linearity (45°, 90°, and especially 200°). Fig. 11 shows the values of all control voltages in the calibrated LUT versus phase setting. Poor P_{LSB} corresponds to one or more control voltages being in the 0.3-0.5 V range, where the varactor gate-to-body bias is 0.2-0 V. This is a region of high slope. To remedy this problem, all tunable capacitors in the reflector should instead be realized using digitally-controlled capacitors, as in [8] and [39]. Switched capacitors can achieve similar capacitor tuning range and Q without a voltage coefficient, which should reduce the AM-PM nonlinearity in this RTPS.

V. CONCLUSION

In this work, a TRM with an LNA, PA, T/R switches, and a single, bidirectional 360° phase-shift RTPS is demonstrated. The RTPS uses an additional series inductor and series varactor in front of a traditional tunable π network to extend the phase-shift range and allow for tuning of both amplitude and phase responses over a broad bandwidth. Compared to the prior-art designs using 360° RTPSs, our TRM is broadband and uses only a single LUT to support the full phase-shift range across a wide frequency range. As such, it is useful for phased arrays that must support broadband modulation and multiple frequency channels with a single calibration.

An ML-based calibration technique for the TRM is introduced that employs Bayesian optimization with both global and local search methods to explore the five-variable control space. This approach minimizes the root mean squared error response of the circuit to achieve accurate, six-bit phase shifting and broadband operation. The ML method is benchmarked against an exhaustive search method, showing that ML can achieve the same accuracy using only 1.5% of the measurements of the exhaustive search method.

TABLE II
PERFORMANCE COMPARISON OF STATE-OF-THE-ART MMWAVE TRM INTEGRATED CIRCUITS

		This work	JSSC'18 [40]	TMTT'19 [41]*	TMTT'19 [42]	JSSC'21 [43]	TMTT'23 [7]	ISSCC'22 [44]	JSSC'22 [45]
Technology		**45 nm SOI**	130 nm SiGe	45 nm SOI	40 nm CMOS	65 nm CMOS	65 nm CMOS	130 nm SiGe	65 nm CMOS
Frequency (GHz)		**27-30**	28-33	24-30	27-30	28	33.5-37.5	24-30	24-29.5
Phase Shifter	Topology	**360° RTPS**	Vector Mod.	Switched LC	Switched LC	PPF+VGA	180° RTPS + Ph.Inv.	180° TLPS + Ph.Inv.	Vector Mod.
	LSB (°)	**5.625**	5.625	11.25	45	11.25	5.625	< 5.625	5.625
	RMSE (°)	**< 1.5 (TX) < 2.8 (RX)**	3.4	< 4	$5^{\#}$	2	2	1.2	< 1.9
	RMSE (dB)	**< 0.4**	0.5	< 0.8	< 0.5	0.4	1	1	0.4-0.5
TX	Gain (dB)	**16.4**	20	16	12.4	25	44	31	25.5
	BW (GHz)	**2.5 (1 dB)**	5 (2 dB)#	6 (3 dB)	3 (3 dB)#	N/A	4 (3 dB)	N/A	5.9 (3 dB)
	oP_{1dB} (dBm)	**11.9-12.9**	10.5	8	> 14.6	13.7	17.2	16	16.0-17.6
	P_{sat} (dBm)	**13.3**	12.5	N/A	15.8	16.1	19.8	17	16.8-18
	P_{DC} (mW)	**$162\text{-}178^{\$}$**	$200^{\$}$	$100^{\$}$	$137^{\$}$	$186^{\dagger}$	$496^{\$}$	$180^{\$}$	$272^{\$}$
RX	Gain (dB)	**16**	20	16.5	16.8	18	26	30	14.2
	BW (GHz)	**3.2 (1 dB)**	5 (2 dB)#	6 (3 dB)	3 (3 dB)#	N/A	4 (3 dB)	N/A	9.6 (3 dB)
	NF (dB)	**3.7-4.1**	4.6	3.7	5.5	4.9	4.2	3.0	4.6
	iP_{1dB} (dBm)	**-23.3**	-22	-15	-16	-29	N/A	-33	-23.7
	P_{DC} (mW)	**30**	130	54	32	88	137	90	82
Active Area/Ch (mm^2)		**0.75**	2.9	3	1	0.48	$3^{\#}$	$1.6^{\#}$	$4^{\#}$

*No T/R switch at the antenna side. #Estimated from figures. $^{\$}$Measured at oP_{1dB}. †Measured at P_{sat}.

Table II summarizes TRM performances of this work compared to the state-of-the-art. Our work achieves comparable RF performances with a small footprint. The proposed TRM meets the phase-shifting specifications for both TX and RX across a wide bandwidth using the same LUT. Although the RTPS varactors affect the system linearity, the issue may be solved by replacing these with digitally controlled capacitors.

APPENDIX

We summarize both the physics-based model and the surrogate model of the circuit to show readers the differences in these two approaches.

A. Physics-Based Model

A simplified schematic of the reflective loads used in the RTPS is shown in Fig. 12. Its load impedance is approximately

$$Z_L(\omega, \boldsymbol{v}) = Z_1(\omega, V_1) + Z_2(\omega, V_2, V_{s2}) \| Z_3(\omega, V_3, V_{s3}), \tag{2}$$

where $\boldsymbol{v}$ is the control-voltage vector and

$$Z_1(\omega, V_1) \approx [j\omega C_{1,(V_1,0)}]^{-1} + R_1 + j\omega L_1, \tag{3}$$
$$Z_2(\omega, V_2, V_{s2}) \approx [j\omega C_{2,(V_2,V_{s2})}]^{-1} + R_2, \tag{4}$$
$$Z_3(\omega, V_3, V_{s3}) \approx [j\omega C_{3,(V_3,V_{s3})}]^{-1} + R_3 + j\omega L_2. \tag{5}$$

Each varactor capacitance has a voltage-dependent behavior modeled as a hyperbolic tangent function [46], as follows:

$$C_{i,(V_i,V_{si})} = C_{fix,i} + C_{tune} \tanh(\alpha V_i - \beta) + V_{s,i} C_{sw,i}, \tag{6}$$

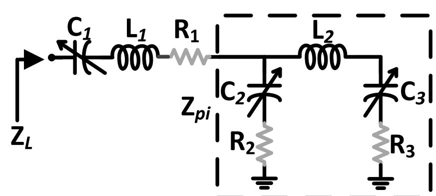

Fig. 12. Simplified schematic of one RTPS load.

where $C_{fix,i}$ is the varactor's fixed capacitance, C_{tune} is how much the capacitance changes, α and β define slope and offset [46], and $C_{sw,i}$ is the switched capacitance.[5]

The behavior of this load can be incorporated into the full TRM response by separating out the reflection coefficient of the RTPS from the rest of the circuit. This yields the TRM's S_{21} response, as follows:

$$S_{21}(\omega, \boldsymbol{v}_p) = G(\omega) e^{j\phi(\omega)} \frac{Z_L(\omega, \boldsymbol{v}_p) - Z_o}{Z_L(\omega, \boldsymbol{v}_p) + Z_o}, \tag{7}$$

where $G(\omega)$ and $\phi(\omega)$ represent the magnitude and phase response of the cascaded circuitry within the TRM excluding the reflection coefficient within the RTPS. This equation shows that the phase and amplitude of the TRM for phase state p can be adjusted by tuning $\boldsymbol{v}_p$ (control voltages for state p).

What makes the calibration of this circuit challenging is finding optimal control voltages that work across the full bandwidth of the circuit and for the desired six-bit resolution. This can be evaluated using the RMS-EVM objective function, ϵ, presented in (1) and written in modified form below,

[5] Z_1 does not include a switched capacitance; hence, its capacitance function is called with $V_{si} = 0$.

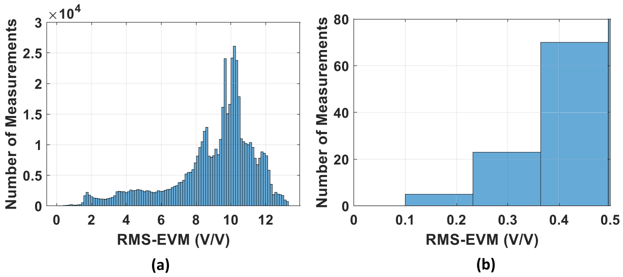

Fig. 13. Histograms of the RMS-EVM for exhaustive search results in one phase state.

normalized by the target gain G_t:

$$\frac{\epsilon(p,\boldsymbol{v})}{G_t} = \sqrt{\frac{1}{N}\sum_{n=1}^{N}\left|1-\frac{S_{21_{meas}}(\omega_n,\boldsymbol{v}_p)}{G_t e^{j(\phi_o - n\cdot\phi_{\delta\omega} - p\cdot\phi_{bit})}}\right|^2}, \quad (8)$$

where $N = 7$ frequency points are averaged in our work. The desired phase response across frequency is represented by $\phi_o - n \cdot \phi_{\delta\omega}$, which includes an offset phase, ϕ_o and the target phase change per frequency step, $\phi_{\delta\omega}$. The desired phase resolution is ϕ_{bit}. The TRM's S_{21} is evaluated across frequency points to create error values for each phase state p, which we wish to minimize by selecting optimum values of $\boldsymbol{v}_p$.

To help illustrate the RMS-EVM objective, Fig. 13 shows histograms of the measured RMS-EVM in one phase state for our exhaustive search. Fig. 13(b) is a zoomed-in version of the region where the RMS-EVM is less than 0.5 V/V. The difficulty in calibration is evidenced by the wide range of possible error values and the small range that achieves the optimum minimum error state.

B. Surrogate Model

The surrogate model is used to model the behavior of the objective function, i.e., $\epsilon(p,\boldsymbol{v})$ in (8) and in Fig. 13). It has a single output, which is the RMS-EVM of the circuit in phase state p, and five inputs, which are the control voltages $\boldsymbol{v} = [V_1, V_2, V_3, V_{s2}, V_{s3}]^\top$. There is no frequency variable within the model. Also, the six-bit phase responses are captured through 64 separate models, each having the objective function modified by ϕ_{bit}, as shown in (8).

Each surrogate is described by a Gaussian process

$$\mathcal{E}_p(\boldsymbol{v_{t+1}}|D_t,) \sim \mathcal{N}(\mu_p(\boldsymbol{v_{t+1}}|D_t), \sigma_p(\boldsymbol{v_{t+1}}|D_t)). \quad (9)$$

We use variable $\mathcal{E}_p$ to show readers that this models the TRM's average error for state p. $\mathcal{E}_p$ has mean, μ_p, and covariance, σ_p, for an arbitrary new vector $\boldsymbol{v_{t+1}}$. Both the mean and variance are augmented by dataset $D_t = \{\boldsymbol{v}_{1:t}, \epsilon_{1:t}\}$ over time to capture new information learned by observing new data points.

The mean function is initialized using a quadratic expression for variables $\boldsymbol{v_i} = [V_1, V_2, V_3, V_{s2}, V_{s3}]^\top$, as follows:

$$m_p(v_{1:t}) = \{v_i^\top A v_i + w^\top v_i + b\}_{i=1}^{t}, \quad (10)$$

where A is a 5×5 symmetric matrix representing the quadratic coefficients for $V_m V_n (m, n \in [1, 2, 3, s2, s3])$, w is a vector of linear coefficients for each set of control voltages v_i, and b is a scalar bias term.

The variance is initiated by calculating the covariance between an initial set of measurements using the first-order differentiable Matérn covariance function, or kernel, $k_{p\_(t)}(v_i, v_j)$ $(i, j \in [1:t])$ [32]. The covariance matrix is created as follows:

$$K_{p\_(t)} = \begin{bmatrix} k_p(v_1,v_1) & k_p(v_1,v_2) & \dots & k_p(v_1,v_t) \\ k_p(v_2,v_1) & k_p(v_2,v_2) & \dots & k_p(v_2,v_t) \\ \vdots & \vdots & \ddots & \vdots \\ k_p(v_t,v_1) & k_p(v_t,v_2) & \dots & k_p(v_t,v_t) \end{bmatrix}. \quad (11)$$

During optimization, the observed data points $\boldsymbol{v}_*$ and corresponding objective values, $\boldsymbol{\epsilon}$, are used to update the posterior mean, variance and covariance matrix ($K_{p\_(t+1)}$), as follows:

$$\begin{aligned} &\mu_p(v_{t+1}|D_t) \\ &= m_p(v_{1:t}) + k_p(v_{t+1}, v_{1:t})^\top \quad (12) \\ &\quad * K_{p\_(t)}(v_{1:t}, v_{1:t})^{-1}\left(\epsilon_{p,1:t} - m_p(v_{1:t})\right), \\ &\sigma_p(v_{t+1}|D_t) \\ &= k_p(v_{t+1}, v_{t+1}) \quad (13) \\ &\quad - k_p(v_{t+1}, v_{1:t}) K_{p\_(t)}(v_{1:t}, v_{1:t})^{-1} k_p(v_{1:t}, v_{t+1}), \\ &K_{p\_(t+1)} \\ &= \begin{bmatrix} K_{p\_(t)} & k_p(v_{1:t}, v_{t+1}) \\ k_p(v_{t+1}, v_{1:t}) & k_p(v_{t+1}, v_{t+1}) \end{bmatrix}. \quad (14) \end{aligned}$$

The surrogate model is updated iteratively, according to the acquisition, iteration, and convergence algorithms discussed in Section III-B.

Acknowledgment

The authors thank IDT (now Renesas) for support and GlobalFoundries for 45RFSOI chip fabrication. This material is based on the work support of its industry members. Finally, they used Grammarly to improve their writing in this manuscript.

References

[1] W. Roh et al., "Millimeter-wave beamforming as an enabling technology for 5G cellular communications: Theoretical feasibility and prototype results," *IEEE Commun. Mag.*, vol. 52, no. 2, pp. 106–113, Feb. 2014.

[2] K.-J. Koh and G. M. Rebeiz, "0.13-μm CMOS phase shifters for X-, Ku-, and K-band phased arrays," *IEEE J. Solid-State Circuits*, vol. 42, no. 11, pp. 2535–2546, Nov. 2007.

[3] M.-D. Tsai and A. Natarajan, "60GHz passive and active RF-path phase shifters in silicon," in *Proc. IEEE Radio Freq. Integr. Circuits Symp.*, Jun. 2009, pp. 223–226.

[4] Y. Chang and B. A. Floyd, "Reduction of phase and gain control dependencies within a 20 GHz beamforming receiver IC," *IEEE Access*, vol. 11, pp. 68066–68078, 2023.

[5] A. Natarajan, M.-D. Tsai, and B. Floyd, "60GHz RF-path phase-shifting two-element phased-array front-end in silicon," in *Proc. Symp. VLSI Circuits*, Jun. 2009, pp. 250–251.

[6] A. Valdes-Garcia et al., "A fully integrated 16-element phased-array transmitter in SiGe BiCMOS for 60-GHz communications," *IEEE J. Solid-State Circuits*, vol. 45, no. 12, pp. 2757–2773, Dec. 2010.

[7] P. Guan et al., "A 33.5–37.5-GHz four-element phased-array transceiver front-end with hybrid architecture phase shifters and gain controllers," *IEEE Trans. Microw. Theory Techn.*, vol. 71, no. 9, pp. 4129–4143, Sep. 2023.

[8] J. Xia, M. Farouk, and S. Boumaiza, "Digitally-assisted 27–33 GHz reflection-type phase shifter with enhanced accuracy and low IL-variation," in *Proc. IEEE Radio Freq. Integr. Circuits Symp. (RFIC)*, Aug. 2019, pp. 63–66.

[9] T.-W. Li and H. Wang, "A millimeter-wave fully integrated passive reflection-type phase shifter with transformer-based multi-resonance loads for 360° phase shifting," *IEEE Trans. Circuits Syst. I, Reg. Papers*, vol. 65, no. 4, pp. 1406–1419, Apr. 2018.

[10] P. Gu and D. Zhao, "Geometric analysis and systematic design of a reflective-type phase shifter with full 360° phase shift range and minimal loss variation," *IEEE Trans. Microw. Theory Techn.*, vol. 67, no. 10, pp. 4156–4166, Oct. 2019.

[11] A. Basaligheh, P. Saffari, S. R. Boroujeni, I. Filanovsky, and K. Moez, "A 28–30 GHz CMOS reflection-type phase shifter with full 360° phase shift range," *IEEE Trans. Circuits Syst. II, Exp. Briefs*, vol. 67, no. 11, pp. 2452–2456, Nov. 2020.

[12] R. Garg and A. S. Natarajan, "A 28-GHz low-power phased-array receiver front-end with 360° RTPS phase shift range," *IEEE Trans. Microw. Theory Techn.*, vol. 65, no. 11, pp. 4703–4714, Nov. 2017.

[13] Y. Chang and B. A. Floyd, "A broadband reflection-type phase shifter achieving uniform phase and amplitude response across 27 to 31 GHz," in *Proc. IEEE BiCMOS Compound Semiconductor Integr. Circuits Technol. Symp. (BCICTS)*, Nov. 2019, pp. 1–4.

[14] A. Natarajan, A. Valdes-Garcia, B. Sadhu, S. K. Reynolds, and B. D. Parker, "W-band dual-polarization phased-array transceiver front-end in SiGe BiCMOS," *IEEE Trans. Microw. Theory Tech.*, vol. 63, no. 6, pp. 1989–2002, Jun. 2015.

[15] T. Wang et al., "Random forest-Bayesian optimization for product quality prediction with large-scale dimensions in process industrial cyber–physical systems," *IEEE Internet Things J.*, vol. 7, no. 9, pp. 8641–8653, Sep. 2020.

[16] C. Li, B. Ustundag, A. Kumar, M. Boenke, U. Kodak, and G. Rebeiz, "$<$ 0.8dB IL 46 dBm OIP3 Ka band SPDT for 5G communication," in *Proc. IEEE 18th Topical Meeting Silicon Monolithic Integr. Circuits RF Syst. (SiRF)*, Jan. 2018, pp. 1–3.

[17] F.-J. Huang and K. O. Kenneth, "A 0.5-μ/m CMOS T/R switch for 900-MHz wireless applications," *IEEE J. Solid-State Circuits*, vol. 36, no. 3, pp. 486–492, Mar. 2001.

[18] M. Parlak and J. F. Buckwalter, "A 2.5-dB insertion loss, DC-60 GHz CMOS SPDT switch in 45-nm SOI," in *Proc. IEEE Compound Semiconductor Integr. Circuit Symp. (CSICS)*, Oct. 2011, pp. 1–4.

[19] M. K. Chirala and B. A. Floyd, "Millimeter-wave Lange and ring-hybrid couplers in a silicon technology for E-band applications," in *IEEE MTT-S Int. Microw. Symp. Dig.*, Jun. 2006, pp. 1547–1550.

[20] S. Weisberg, *Applied Linear Regression*. Hoboken, NJ, USA: Wiley, 2005.

[21] A. H. Victoria and G. Maragatham, "Automatic tuning of hyperparameters using Bayesian optimization," *Evolving Syst.*, vol. 12, no. 1, pp. 217–223, 2021.

[22] H. M. Torun, M. Swaminathan, A. K. Davis, and M. L. F. Bellaredj, "A global Bayesian optimization algorithm and its application to integrated system design," *IEEE Trans. Very Large Scale Integr. (VLSI) Syst.*, vol. 26, no. 4, pp. 792–802, Apr. 2018.

[23] Y. Wang, P. D. Franzon, D. Smart, and B. Swahn, "Multi-fidelity surrogate-based optimization for electromagnetic simulation acceleration," *ACM Trans. Des. Autom. Electron. Syst.*, vol. 25, no. 5, pp. 1–21, Jul. 2020.

[24] W. Lyu, F. Yang, C. Yan, D. Zhou, and X. Zeng, "Batch Bayesian optimization via multi-objective acquisition ensemble for automated analog circuit design," in *Proc. Int. Conf. Mach. Learn.*, 2018, pp. 3306–3314.

[25] M. Liu et al., "Closing the design loop: Bayesian optimization assisted hierarchical analog layout synthesis," in *Proc. 57th ACM/IEEE Design Autom. Conf. (DAC)*, Jul. 2020, pp. 1–6.

[26] S. Zhang et al., "An efficient multi-fidelity Bayesian optimization approach for analog circuit synthesis," in *Proc. 56th ACM/IEEE Design Autom. Conf. (DAC)*, Jun. 2019, pp. 1–6.

[27] R. Pan, J. Tao, Y. Su, D. Zhou, X. Zeng, and X. Li, "Analog/RF post-silicon tuning via Bayesian optimization," *ACM Trans. Design Autom. Electron. Syst.*, vol. 25, no. 1, pp. 1–17, Jan. 2020.

[28] J. Huang, Z. Fan, and J. Cai, "Design of a high-efficiency sequential load modulated balanced amplifier based on multiple multiobjective Bayesian optimization," *IEEE Trans. Comput.-Aided Design Integr. Circuits Syst.*, vol. 43, no. 12, pp. 4348–4360, Dec. 2024.

[29] F. Archetti, A. Candelieri, F. Archetti, and A. Candelieri, "The surrogate model," in *Bayesian Optimization and Data Science*, 2019, pp. 37–56. AQ:3

[30] C. K. Williams and C. E. Rasmussen, *Gaussian Processes for Machine Learning*, vol. 2. Cambridge, MA, USA: MIT Press, 2006.

[31] Z. Wang, M. Zoghi, F. Hutter, D. S. Matheson, and N. de Freitas, "Bayesian optimization in high dimensions via random embeddings," in *Proc. IJCAI*, Aug. 2013, pp. 361–387.

[32] A. Melkumyan and F. Ramos, "Multi-kernel Gaussian processes," in *Proc. IJCAI*, Jul. 2011, pp. 1408–1413.

[33] H. Wang, B. van Stein, M. Emmerich, and T. Back, "A new acquisition function for Bayesian optimization based on the moment-generating function," in *Proc. IEEE Int. Conf. Syst., Man, Cybern. (SMC)*, Oct. 2017, pp. 507–512.

[34] S. Zhang, F. Yang, D. Zhou, and X. Zeng, "An efficient asynchronous batch Bayesian optimization approach for analog circuit synthesis," in *Proc. 57th ACM/IEEE Design Autom. Conf. (DAC)*, Dec. 2020, pp. 1–6.

[35] R. Zhong, E. Zhang, and M. Munetomo, "Accelerating the evolutionary algorithms by Gaussian process regression with ϵ-greedy acquisition function," 2022, *arXiv:2210.06814*.

[36] N. Srinivas, A. Krause, S. M. Kakade, and M. W. Seeger, "Information-theoretic regret bounds for Gaussian process optimization in the bandit setting," *IEEE Trans. Inf. Theory*, vol. 58, no. 5, pp. 3250–3265, May 2012.

[37] P. Rantalankila, J. Kannala, and E. Rahtu, "Generating object segmentation proposals using global and local search," in *Proc. IEEE Conf. Comput. Vis. Pattern Recognit.*, Jun. 2014, pp. 2417–2424.

[38] W.-L. Loh, "On Latin hypercube sampling," *Ann. Statist.*, vol. 24, no. 5, pp. 2058–2080, 1996.

[39] P. Guan, H. Jia, W. Deng, Z. Wang, and B. Chi, "A 33.5–37.5 GHz 4-element phased-array transceiver front-end with high-accuracy low-variation 6-bit resolution 360° phase shift and 0 31.5 dB gain control in 65 nm CMOS," in *Proc. IEEE Asian Solid-State Circuits Conf. (A-SSCC)*, Nov. 2021, pp. 1–3.

[40] K. Kibaroglu, M. Sayginer, and G. M. Rebeiz, "A low-cost scalable 32-element 28-GHz phased array transceiver for 5G communication links based on a 2×2 beamformer flip-chip unit cell," *IEEE J. Solid-State Circuits*, vol. 53, no. 5, pp. 1260–1274, May 2018.

[41] U. Kodak and G. M. Rebeiz, "A 5G 28-GHz common-leg T/R front-end in 45-nm CMOS SOI with 3.7-dB NF and -30-dBc EVM with 64-QAM/500-MBaud modulation," *IEEE Trans. Microw. Theory Techn.*, vol. 67, no. 1, pp. 318–331, Jan. 2019.

[42] S. Shakib, M. Elkholy, J. Dunworth, V. Aparin, and K. Entesari, "A wideband 28-GHz transmit-receive front-end for 5G handset phased arrays in 40-nm CMOS," *IEEE Trans. Microw. Theory Techn.*, vol. 67, no. 7, pp. 2946–2963, Jul. 2019.

[43] J. Pang et al., "A CMOS dual-polarized phased-array beamformer utilizing cross-polarization leakage cancellation for 5G MIMO systems," *IEEE J. Solid-State Circuits*, vol. 56, no. 4, pp. 1310–1326, Apr. 2021.

[44] B. Sadhu et al., "A 24-to-30GHz 256-element dual-polarized 5G phased array with fast beam-switching support for >30,000 beams," in *IEEE Int. Solid-State Circuits Conf. (ISSCC) Dig. Tech. Papers*, vol. 65, Feb. 2022, pp. 436–438.

[45] Y. Yi et al., "A 24–29.5-GHz highly linear phased-array transceiver front-end in 65-nm CMOS supporting 800-MHz 64-QAM and 400-MHz 256-QAM for 5G new radio," *IEEE J. Solid-State Circuits*, vol. 57, no. 9, pp. 2702–2718, Sep. 2022.

[46] P. Sameni et al., "Characterization and modeling of accumulation-mode MOS varactors," in *Proc. Can. Conf. Electr. Comput. Eng.*, May 2005, pp. 1554–1557.

Yuan Chang received the double B.S. degree (Hons.) in electrical engineering from Beijing University of Post and Telecommunications (BUPT), China, and the Queen Mary University of London, U.K., in 2013, the M.S. degree in electrical engineering from BUPT in 2016, and the Ph.D. degree in electrical engineering from NC State University, Raleigh, NC, USA, in 2023. He was an Exchange Researcher at Aalto University, Finland, in 2015. His research interests include RF and mmWave circuits and phased-array calibrations. He received the Analog Devices Outstanding Student IC Designer Award in 2018.

Yuejiang Wen (Graduate Student Member, IEEE) received the B.E. degree in optoelectronic information science and engineering and the M.Sc. degree in optical engineering from the University Electronic Science and Technology of China (UESTC), Chengdu, China, in 2012 and 2015, respectively, and the second M.Sc. degree in electrical engineering from Clemson University, Clemson, SC, USA, in 2018. He is currently pursuing the Ph.D. degree in electrical and computer engineering with NC State University, Raleigh, NC, USA.

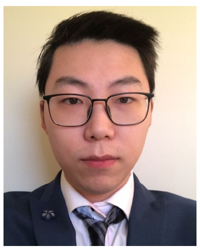

Zhangjie Hong (Graduate Student Member, IEEE) received the B.S. degree in information engineering from Shanghai Jiao Tong University, Shanghai, China, in 2016, and the Ph.D. degree from NC State University, Raleigh, NC, USA, in 2023. He is currently with Apple Inc. His research interests include phased-array built-in characterization and calibration.

Bharadwaj Padmanabhan (Graduate Student Member, IEEE) received the B.Tech. degree in electronics and communication engineering from SASTRA University, India, in 2020. He is currently pursuing the Ph.D. degree with NC State University, Raleigh, NC, USA. His research interests include software-defined radios, tunable filters, and phased arrays. He received the Analog Devices Outstanding Student Designer Award in 2023.

Paul D. Franzon (Fellow, IEEE) received the B.S., B.E. (Hons.), and Ph.D. degrees from The University of Adelaide, Adelaide, SA, Australia, in 1983, 1984, and 1989, respectively. He has been with AT&T Bell Laboratories, Holmdel, NJ, USA; DSTO Australia, Salisbury, SA, Australia; and Australia Telecom, Adelaide. He co-founded four companies: Communica, Adelaide; LightSpin Technologies, Bethesda, MD, USA; Indago, Raleigh, NC, USA; and Polymer Braille Inc., Raleigh. He served with the Australian Army Reserve for 13 years as an Infantry Soldier and Officer. He is currently the Cirrus Logic Distinguished Professor and the Director of the Graduate Programs in Electrical and Computer Engineering, NC State University, Raleigh. His current research interests include the technology, design, and EDA of complex microsystems incorporating VLSI, advanced packaging, machine learning, and nanoelectronics. He has led major efforts and authored over 300 articles in these areas. He received the NSF Young Investigators Award in 1993, the NC State Outstanding Teachers in 2001, and the Alcoa Research Award in 2005.

Brian A. Floyd (Senior Member, IEEE) received the B.S. (Hons.), M.Eng., and Ph.D. degrees in electrical and computer engineering from the University of Florida, Gainesville, FL, USA, in 1996, 1998, and 2001, respectively.

From 2001 to 2009, he was with the IBM Thomas J. Watson Research Center, Yorktown Heights, NY, USA, as a Research Staff Member and then the Manager of the Wireless Circuits and Systems Group, investigating 60 GHz radios and phased arrays. In 2010, he joined NC State University, Raleigh, NC, USA, where he is the Alton and Mildred Lancaster Professor of electrical and computer engineering and a University Faculty Scholar. He has contributed over 135 articles and 34 patents. His research interests include RF and millimeter-wave circuits for communications and sensing applications.

Dr. Floyd received the 2023 NC State Innovator of the Year Award, the 2016 NC State Outstanding Teacher Award, the 2011 DARPA Young Faculty Award, and the Best Paper Awards from the International Solid-State Circuits Conference and IBM. He has served on the Administrative Committee for the IEEE Solid-State Circuits Society, the editorial board for IEEE JOURNAL OF SOLID-STATE CIRCUITS, the advisory board for Lumeova Inc., a technical advisory board for the Semiconductor Research Corporation, the Executive Committees for the IEEE RFIC Symposium, and the Technical Program Committee (TPC) for multiple IEEE conferences. In addition, he served as the TPC Chair and the General Chair of the IEEE RFIC Symposium in 2020 and 2021, respectively.